Hydrogen-barrier coatings against dual-atmosphere corrosion for IT-SOFC interconnect applications

Citation for the original published paper (version of record):
Tomas, M., Svensson, J., Froitzheim, J. (2024). Hydrogen-barrier coatings against dual-atmosphere corrosion for IT-SOFC interconnect
applications. International Journal of Hydrogen Energy, 58: 852-862.
http://dx.doi.org/10.1016/j.ijhydene.2024.01.219

(article starts on next page)

International Journal of Hydrogen Energy 58 (2024) 852–862

Contents lists available at ScienceDirect

International Journal of Hydrogen Energy

journal homepage: www.elsevier.com/locate/he

Hydrogen-barrier coatings against dual-atmosphere corrosion for IT-SOFC interconnect applications

M. Tomas *, J.-E. Svensson, J. Froitzheim

Chemistry and Chemical Engineering, Chalmers University of Technology, Kemivägen 10, 41296, Gothenburg, Sweden

ARTICLE INFO

Handling Editor: Fanglin F. Chen

Keywords:
Dual-atmosphere
Interconnect
Coatings
Area-specific resistance
SOFC
Hydrogen barrier

ABSTRACT

A key component of a Solid Oxide Fuel Cell (SOFC) is the interconnect, which connects individual fuel cells in series to form a fuel cell stack. The interconnect is exposed to air and fuel in parallel; these so-called dual-atmosphere conditions cause severe corrosion on the air-side. This work investigates interconnect coatings that can mitigate this effect. Physical Vapour Deposition (PVD) coatings of Cr_2O_3, CeO_2, YSZ, and Al_2O_3 on ferritic stainless steel (AISI 441) were exposed under dual-atmosphere conditions for up to 3000 h. The evolution of the corrosion products was evaluated using optical microscopy and Scanning Electron Microscopy (SEM) in combination with Energy-dispersive x-ray Spectroscopy (EDS). The SEM analysis showed that a chromia coating was not sufficient to reduce the dual-atmosphere effect, while other coatings on the fuel-side suppressed the dual-atmosphere effect by forming a barrier to hydrogen permeation. The best outcomes were observed with Al_2O_3 coatings on the fuel-side, which drastically reduced the dual-atmosphere effect. A 30 nm Al_2O_3 coating displayed acceptable Area-Specific Resistance (ASR).

1. Introduction

In recent years, extensive research efforts have focused on improving the performance, durability, and cost-effectiveness of Solid Oxide Fuel Cells (SOFCs). Researchers have explored various aspects of the SOFC technology, including the materials, cell design, and system integration [1–4]. One area of research has been the development of metallic interconnects. These interconnects are essential for achieving the desired electrical potential and for facilitating the flow of electrical current between the cells. Metallic interconnects offer certain advantages over ceramic counterparts, such as lower costs ease of manufacturing. However, they are also subject to corrosion, resulting in increasing electrical resistance, and material stability challenges under the harsh operating conditions of SOFCs. One of the primary considerations for metallic interconnects is their stability in the face of high-temperature oxidation. The interconnect materials must withstand exposure to oxidising and reducing atmospheres, high temperatures (typically 600°C-800 °C), and long-term operation. Commonly used metallic interconnect materials include ferritic stainless steels, such as Crofer 22 APU and AISI 441, owing to their favourable high-temperature oxidation resistance profiles, thermal expansion coefficients that match those of other cell components, and reasonable costs.

However, metallic interconnects are susceptible to degradation processes, such as Cr evaporation and the dual-atmosphere effect. Cr(VI) evaporation from the steel can poison the cathode, thereby reducing cell performance and durability [5–8]. Furthermore, this depletes the interconnect of Cr, which may result in Fe oxide formation. The formation and growth of a Cr_2O_3 scale on the interconnect surface increases its electrical resistance, impairing the overall performance of the fuel cell [9]. Various approaches have been explored to mitigate these challenges, so as to enhance the performance and durability of metallic interconnects. These measures include the development of protective coatings, alloy modifications, and surface treatments. Protective coatings, such as manganese (Mn)- and cobalt (Co)-based spinels [5,10–18], have demonstrated effectiveness in reducing Cr(VI) evaporation and improving interconnect stability. Reactive elements, such as cerium (Ce), have been investigated for their beneficial effects on Cr_2O_3-forming alloys, including selective chromium oxidation and scale growth rate reduction [19–22].

The dual-atmosphere effect, particularly at intermediate temperatures (around 600 °C), is a significant concern for metallic interconnects [23,24]. When exposed to air and fuel gases simultaneously, the interconnect experiences different chemical reactions, leading to complex corrosion processes. Yang et al. [25,26] have observed that an alloy

* Corresponding author.
E-mail address: tommat@chalmers.se (M. Tomas).

https://doi.org/10.1016/j.ijhydene.2024.01.219
Received 30 November 2023; Received in revised form 11 January 2024; Accepted 19 January 2024
Available online 30 January 2024

Table 1
Composition of the studied steel (in wt%), as specified by the manufacturer.

Materials	Fe	Cr	C	Mn	Si	Ni	Ti	Nb	Al	N	P	S
AISI 441	Bal.	17.53	0.016	0.40	0.59	0.15	0.172	0.41	0.007	0.015	0.024	<0.001

Table 2
Experimental matrix of the coating systems used and their exposure times.

Coating on the fuel-side	Thickness (nm)	Exposure time (h)
Uncoated	/	1000
Cr_2O_3	~200	1000
CeO_2	~50	1000
CeO_2	~200	1000
YSZ	~50	1000
YSZ	~200	1000
Al_2O_3	~30	3000
Al_2O_3	~100	3000
Al_2O_3	~300	3000
Al_2O_3	~600	3000

exposed to dual-atmosphere conditions behaves differently from an alloy that is exposed to single-atmosphere conditions. Although it has been commonly accepted that diffusion of hydrogen from the fuel-side to the air-side influences the oxidation process, the mechanism behind the breakdown of the oxide scale is not fully understood. Moreover, the reported severity of the dual-atmosphere effect varies widely among different studies [24,27–29]. At high temperatures (800°C-850 °C), several authors [25,26,30,31] have noted iron enrichment of the protective scale on the air-side. At lower temperatures (600°C-700 °C), the air-facing side of the sample undergoes severe corrosion, with the formation of hematite nodules and, over time, the formation of a thick hematite oxide layer [32–34]. Since iron oxides are poorly protective, the scale grows several orders of magnitude faster than chromium oxide, leading to faster material degradation and loss of performance. This phenomenon has been observed for various alloys, such as AISI 441 [23,24,35], AISI 430 [36,37], Sanergy HT [38], and Crofer APU 22 [39], to cite the alloys most commonly used for interconnect applications. Other researchers [40] have proposed that a higher Cr concentration in the alloy may help reduce the dual-atmosphere effect by slowing hydrogen diffusion [26,34]. Several explanations for this phenomenon have been put forward. Rufner et al. [28] have suggested that the partial pressure of oxygen (pO_2) on the air-side could be locally modified by the permeating hydrogen. Yang et al. [26] have suggested that it may be due to an increased number of cation vacancies in proximity to the air-side, leading to hydroxide species formation, which would enhance the growth rate of the scale. Other authors [41] have proposed theories in which the lattice is distorted due to the presence of hydrogen. Recently, Gunduz et al. [33] have argued against the above mentioned mechanisms, instead they have suggested that the effect of hydrogen on Cr_2O_3 scale protectiveness is related to the reduction in Cr transport along the grain boundaries.

A common factor in the afore-mentioned studies is the uncoated fuel-side of the sample. Research conducted by Goebel et al. [35] has shown the efficiency of pre-oxidation of the sample, especially on the fuel-side, for delaying the onset of the breakaway oxidation. The longer time that the sample is pre-oxidised, the longer it can sustain the dual-atmosphere effect, indicating the importance of a protective oxide layer on the fuel-side of the sample. Nevertheless, pre-oxidation does not seem to solve the problems of dual-atmosphere corrosion on the long-term [33,42,43]. Tomas et al. [43] showed that even 5h of pre-oxidation at 800 °C was not sufficient to inhibit dual-atmosphere corrosion. Kurokawa et al. [44] showed that chromia reduces hydrogen permeation by four orders of magnitude at 800 °C. However, hydrogen will still permeate through the oxide scale and induce the dual-atmosphere effect. In the present study, we investigate fuel-side coatings and their effectiveness to mitigate dual-atmosphere corrosion due to their hydrogen barriers properties.

In this work, barrier coatings to reduce the dual-atmosphere corrosion for Intermediate-Temperature Solid Oxide Fuel Cells (IT-SOFCs) are investigated. This work evaluates the efficiencies of fuel-side AISI 441 samples coated with Cr_2O_3, CeO_2, YSZ, and Al_2O_3 with respect to reducing the dual-atmosphere effect, as well as electrical resistance. Different coating thicknesses are investigated.

2. Materials and methods

2.1. Sample characteristics and preparation

The composition and characteristics of the material used in this study are described in Table 1 and Table 2.

Samples were coated by the company Alleima AB using a proprietary PVD process. Coin-shaped samples (Ø 21 mm) were stamped out of a metal sheet (0.3 mm thickness) using a hydraulic press. The experimental matrix and exposure characteristics are listed in Table 2. An ultrasonic cleaning procedure that consisted of a bath for 20 min in acetone and 20 min in ethanol was performed before any thermal treatment. All the samples were then pre-oxidised at 800 °C ± 5 °C for 20 min in air +3 % H_2O with a ramp rate of 5C min^{-1} up and down, under a flow rate of 280 mL min^{-1}.

2.2. Dual-atmosphere exposures

All the dual-atmosphere experiments were conducted using the experimental set-up described by Alnegren et al. [23]. The sample holder construction is based on a design by Montana State University, and further information on this set-up can be found elsewhere [28]. Gold rings were used as gaskets for the circular samples, to ensure a gas-tight seal. All of the coin-shaped samples were exposed to a humid dual-atmosphere at 600 °C. The following gas mixtures were used: Ar – 5 % H_2 – 3 % H_2O at a flow rate of 120 smL•min^{-1} on the fuel-side; and air +3 % H_2O at a flow rate of 8800 smL•min^{-1} on the air-side. To adjust the humidity level to 3 %, all gas mixtures were bubbled through a heated water bath and subsequently through a temperature-controlled reflux condenser set to 24.4 °C. All exposures were conducted at a temperature of 600 °C ± 5 °C. The exposures were ended after 1000 h for the uncoated and the Cr_2O_3-, CeO_2-, and yttria-stabilised zirconia (YSZ)-coated samples, and after 3000 h for the Al_2O_3-coated samples.

2.3. Analysis

Photographs of the samples were taken after different exposure times using a Nikon SMZ800 camera equipped with a ring light. For the cross-sectional analyses, the samples were cut with an oil-free, low-speed saw (Struers Minitom). Cross-sections of all the samples were then prepared using a Leica EM TIC 3X Broad Ion Beam (BIB) with an acceleration voltage of 8 kV and a current of 3 mA. The resulting cross-sections were analysed using the JEOL 7800F Prime SEM. Imaging was performed with an acceleration voltage of 10 kV, and Energy-Dispersive x-ray (EDX) analysis was performed with an acceleration voltage of 20 kV.

2.4. Area-Specific Resistance measurement

To determine the Area-Specific Resistance (ASR) contribution of the fuel-side coatings, selected samples were pre-oxidised according to the

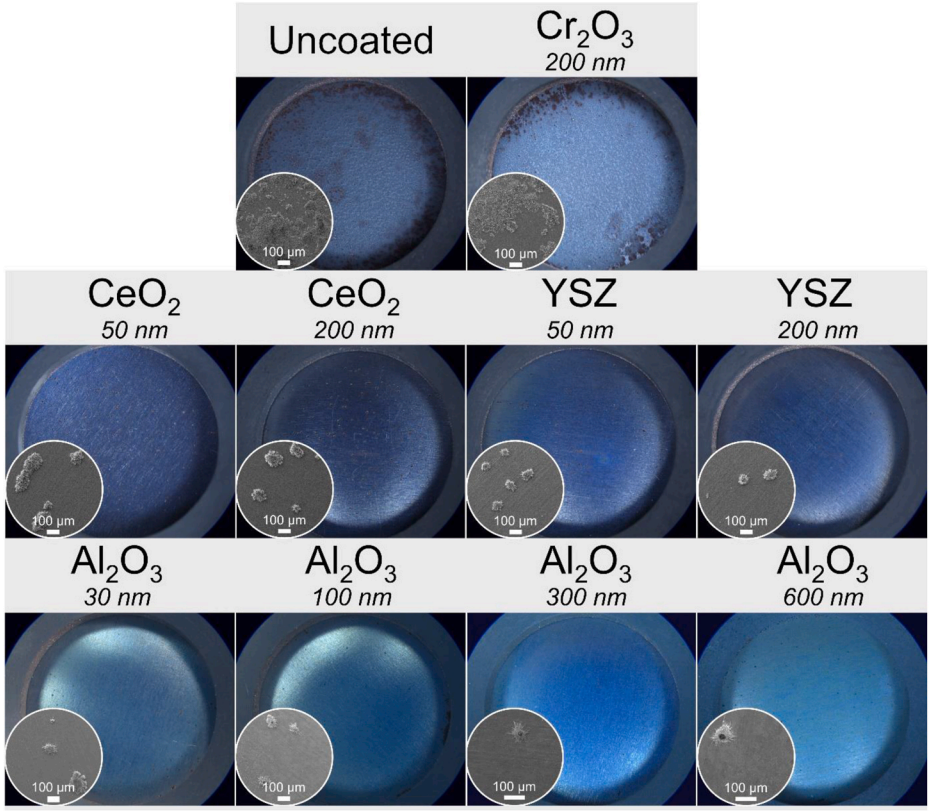

Fig. 1. Photographs of the air-facing sides of selected alloys exposed to dual-atmosphere conditions (Ar-5% H_2 + 3 % H_2O//Air + 3 % H_2O) at 600 °C for 1000 h (value indicated underneath each coating label is the thickness of the coating). The insets show high-magnification SEM images. In the cases of the Al_2O_3 coatings, the SEM images represent the samples exposed for 3000 h, as the exposures were continued because the Al_2O_3-coated samples exhibited the best behaviours against the dual-atmosphere effect.

procedure described above and thereafter exposed for 500 h under the single-atmosphere condition (Ar – 5 % H_2 + 3 % H_2O) at a flow rate of 400 smL•min^{-1} at 600 °C. The ASR is the measured resistance (R) multiplied by the contact area (A). A sputter mask with an opening of 10 × 10 mm^2 was placed on the sample, which was then coated with gold for 2 min using the Quorum 150 sputter coater and a sputtering current of 60 mA. This procedure was repeated for the reverse side of the sample. The sputtering step was used to produce electrodes with a defined area. The samples were then painted with Metalor M − 9875 gold paint. Sintering of the gold paint was achieved in a two-step process: a drying step for 10 min at 150 °C; and a sintering step for 1 h at 600 °C. This ensured good contact between the sample and the platinum electrodes. The exposed samples were then mounted in a ProboStat™ (NorECs, Norway) measurement set-up using a 1-cm^2 platinum wire and grid to contact the sample electrodes and a Keithley 2400 source meter. The applied current was set to 100 mA cm^{-2}. The resistance was measured by the 2-point, 4-wire method at 600 °C in Ar – 5 % H_2 + 3 % H_2O for 1 h. During the subsequent cooling of the sample, the ASR was monitored to check for semi-conductive behaviour. The uncoated side of the sample was ground before the gold sputtering, so as to minimise the contribution of that surface; as a consequence, the obtained values were not divided by two.

3. Results

3.1. Overview of the samples

Fig. 1 shows an overview of the air-sides of the different samples exposed for 1000 h at 600 °C under dual-atmosphere conditions. Apart from the uncoated sample used as reference, the 200 nm Cr_2O_3 coating was tested because pre-oxidation has been shown to minimise the ingress of hydrogen. The CeO_2 coating was chosen as barrier material because of its acceptable conductivity at low pO_2. YSZ and Al_2O_3 were chosen because of their hydrogen barrier properties. The uncoated and Cr_2O_3-coated samples both show severe corrosion, as almost the entire sample surface is covered with a non-protective, Fe-rich oxide scale. The thicker chromia scale applied by PVD does not seem to slow hydrogen permeation to a sufficient degree to preserve the protective behaviour on the air-facing side of the sample. The CeO_2-coated samples suffer milder corrosion. Some Fe-rich nodules can be observed on the surfaces of these samples. Based on visual examination, both CeO_2-coated samples exhibit a similar level of corrosion, regardless of the coating thickness. The YSZ-coated samples show lower corrosion levels compared to the CeO_2-coated samples. From a visual analysis, the thicker YSZ coating (200 nm) seems to be more effective at reducing the ingress of hydrogen, as the sample shows fewer Fe-rich nodules compared to its thinner counterpart (50 nm YSZ coating). After 1000 h of exposure under dual-atmosphere conditions, the thicker Al_2O_3 coatings (~300 nm and~600 nm) show minimal corrosion, while the thinner coatings (~30 nm and~100 nm) exhibit slightly more Fe-rich nodules.

3.2. Uncoated and chromia-coated steel

Fig. 2 shows the SEM micrographs of the uncoated and Cr_2O_3-coated samples. The top-views of the air-side of both the uncoated and Cr_2O_3-coated samples (Fig. 2a and b) show a mostly corroded surface that is covered by an Fe-rich oxide layer. A thin Cr-rich layer is still visible on a small area of the sample surface for both the uncoated and Cr_2O_3-coated samples. The cross-section of the air-facing side of the uncoated sample (Fig. 2e) reveals a thick oxide scale (~40 µm), composed of an outer Fe-rich oxide that is roughly 20 µm in thickness, and an inner $(Fe,Cr)_3O_4$

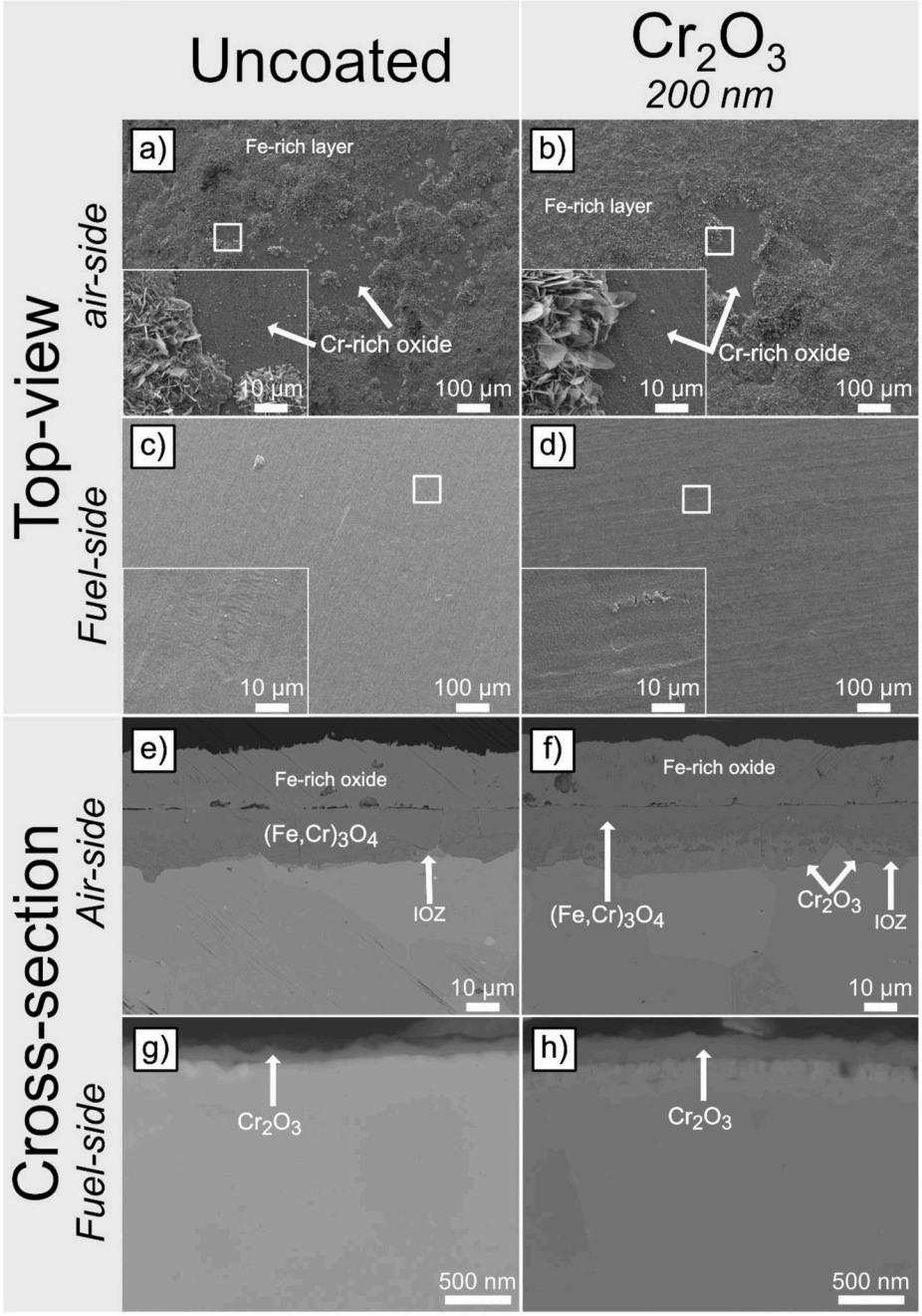

Fig. 2. SEM micrographs of the top-views of the air-side of: a) the uncoated sample, and b) Cr_2O_3-coated sample; the top-views of the fuel-side of: c) the uncoated sample and d) the Cr_2O_3-coated sample; cross-sections of the air-side of: e) the uncoated sample and f) the uncoated sample; and cross-sections of the fuel-side of g) the uncoated sample, and h) the Cr_2O_3-coated sample, all of which were pre-oxidised for 20 min at 800 °C and exposed to the dual-atmosphere (Ar-5% H_2 + 3 % H_2O//Air + 3 % H_2O) for 1000 h at 600 °C. Insets: Higher-magnification images of selected scale regions.

spinel (~20 μm in thickness). A small Internal Oxide Zone (IOZ) is observed underneath the spinel. Previous studies [23,28] have documented the presence of similar corrosion products on AISI 441 that was exposed to dual-atmosphere conditions. Fig. 2f shows the cross-section of the air-side of the Cr_2O_3-coated sample. On the sample surface, there is a thick (~40 μm) oxide layer that is composed of a Fe-rich oxide scale, roughly 20 μm in thickness, and underneath this layer is a 20-μm-thick $(Fe,Cr)_3O_4$ spinel. Beneath the spinel lies an IOZ that is partially encapsulated by a thin Cr_2O_3 layer.

The top-view images of the fuel-side of the sample (see Fig. 2c and d) show a homogeneous Cr_2O_3 oxide layer covering the sample surface in both cases. The cross-section of the fuel-side of the uncoated sample (see Fig. 2g) shows a thin (<100 nm) and continuous Cr_2O_3 layer. The fuel-side of the Cr_2O_3-coated sample (Fig. 2h) exhibits a homogeneous Cr_2O_3 layer that is roughly 200 nm in thickness.

Those observations are in accordance with the results of previous studies [23,35] showing that uncoated AISI 441 ferritic stainless steel suffers severe corrosion after 1000 h of exposure at 600 °C under dual-atmosphere conditions, even when the steel sample is pre-oxidised. A thick, Fe-rich oxide scale is identified on the surface of the air-side of the sample. The pre-oxidation step is designed to simulate the conditioning of the stack before operation. Furthermore, it is expected to generate a protective Cr_2O_3 layer that acts as a diffusion barrier to both oxidation of the alloy and the transport of hydrogen from the fuel-side to

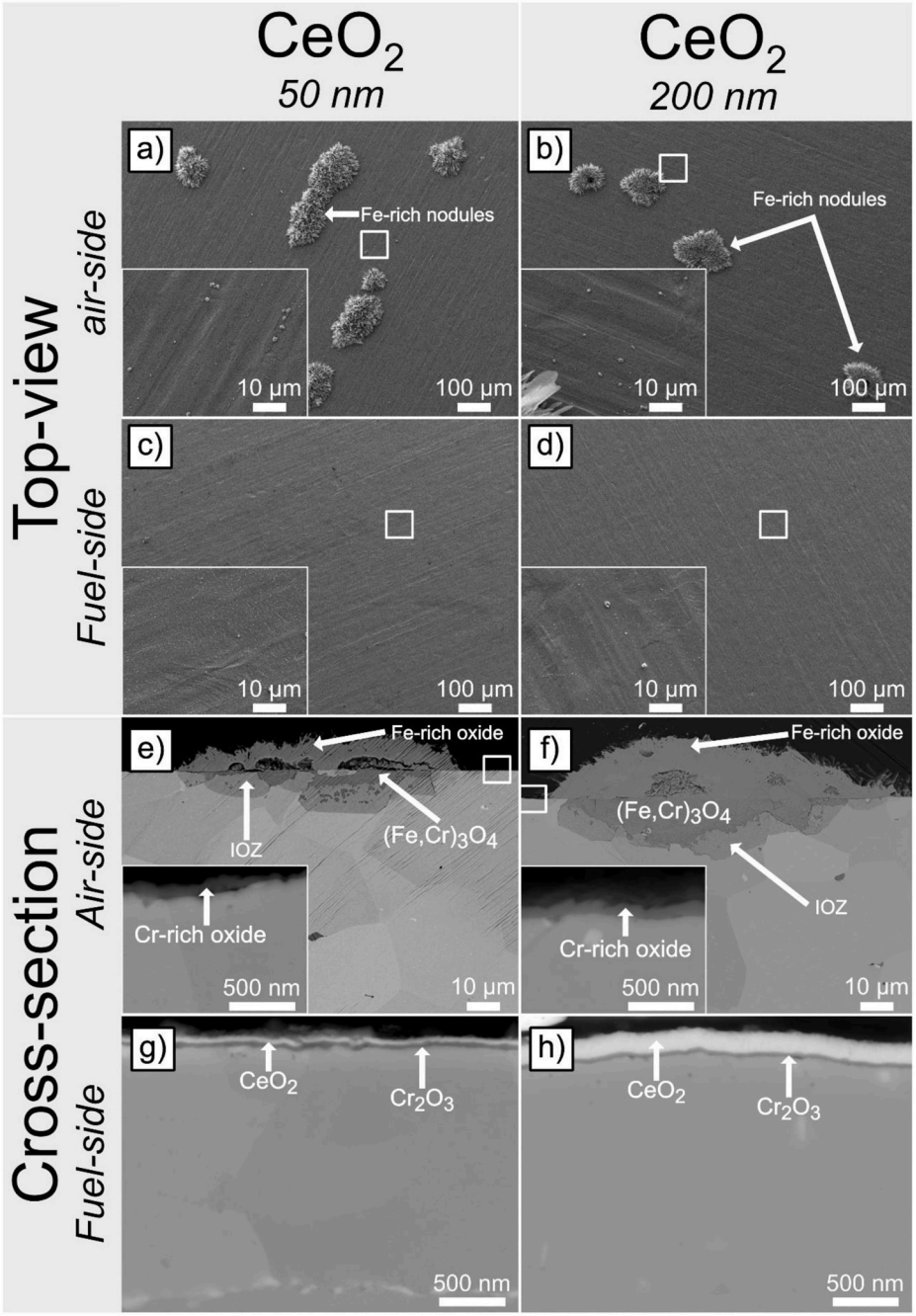

Fig. 3. SEM micrographs of CeO_2-coated samples representing the top-views of the air-side of: a) the 50 nm CeO_2-coated sample and b) the 200 nm CeO_2-coated sample; the top-views of the fuel-side of: c) the 50 nm CeO_2-coated sample and d) the 200 nm CeO_2-coated sample; the cross-sections of the air-side of: e) the 50 nm CeO_2-coated sample and f) the 200 nm CeO_2-coated sample; and the cross-sections of the fuel-side of: g) the 50 nm CeO_2-coated sample and h) the 200 nm CeO_2-coated sample, all of which were pre-oxidised for 20 min at 800 °C and exposed to the dual-atmosphere (Ar-5% H_2 + 3 % H_2O//Air + 3 % H_2O) for 1000 h at 600 °C. Insets: Higher-magnification images of selected scale regions.

the air-side. Kurokawa et al. [44] exposed Fe–16Cr steel at 800 °C and showed that after a continuous thermally grown chromia layer had formed, the permeation of hydrogen was reduced by four orders of magnitude.

Despite having a thicker Cr_2O_3 layer on the fuel-side, the PVD Cr_2O_3-coated sample suffers a similar level of corrosion to that of the uncoated sample. This indicates that PVD-coated Cr_2O_3 is not sufficient to mitigate the dual-atmosphere corrosion effect. The exact mechanism of hydrogen permeation through an oxidised ferritic stainless steel is unknown, however is it commonly speculated that hydrogen permeates as protons through the Cr_2O_3 layer while transport through the metal is attributed to atomic hydrogen transport [44,45–47].

3.3. Ceria-coated steel

Fig. 3 depicts the SEM micrographs of the samples that were coated with either 50 nm or 200 nm CeO_2. Fig. 3a and b shows the top-views of the air-facing sides of the samples. The sample surfaces are mostly covered by a protective Cr-rich oxide layer with some Fe-rich nodules, which are approximately 100 µm in diameter. Slightly more Fe-rich nodules can be observed on the 50 nm CeO_2-coated sample, in accordance with the optical images in Fig. 1. In the cross-section of the air-

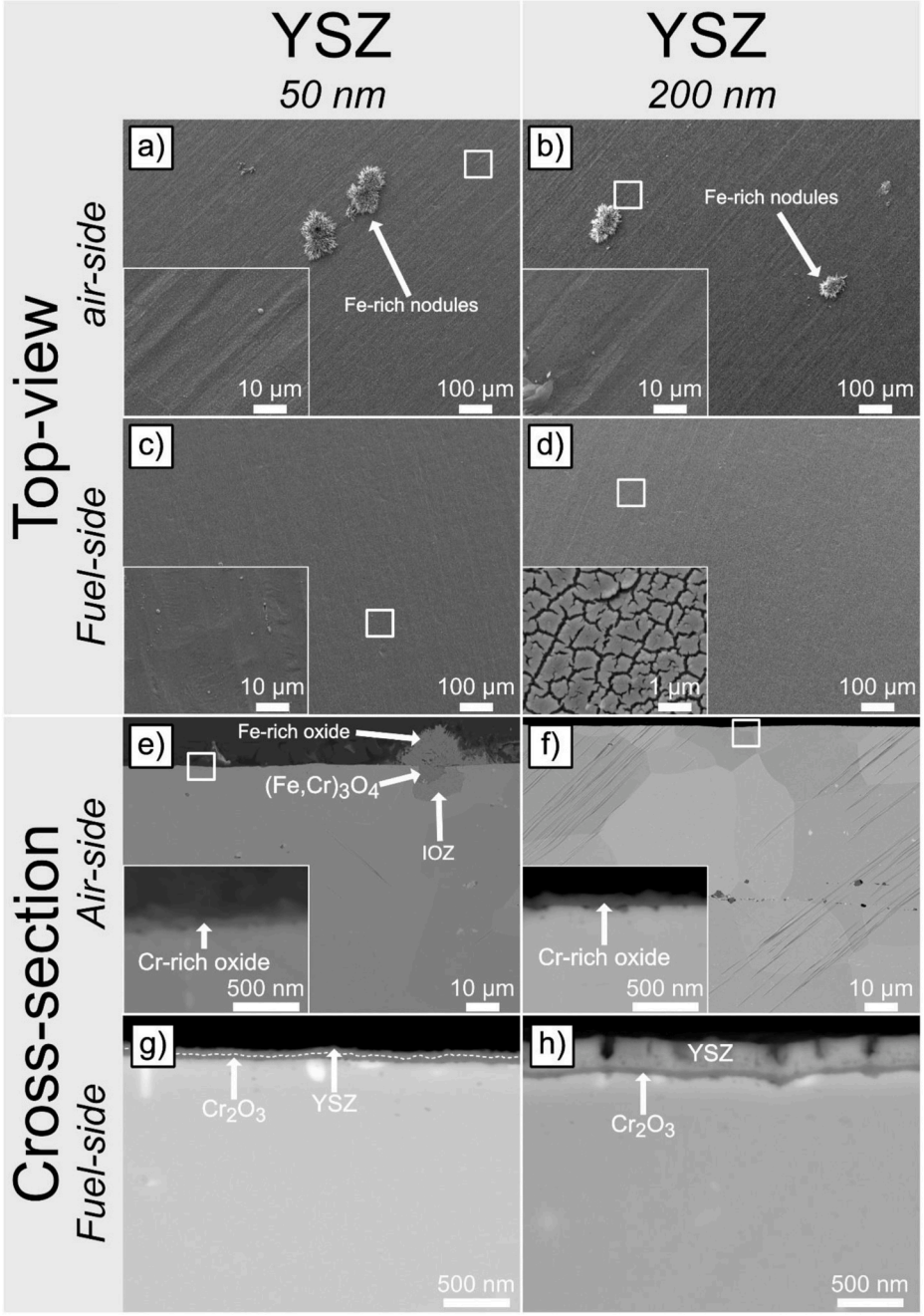

Fig. 4. SEM micrographs of YSZ-coated samples representing the top-views of the air-side of: a) the 50 nm YSZ-coated sample and b) the 200 nm YSZ-coated sample; the top-views of the fuel-side of c) the 50 nm YSZ-coated sample and d) the 200 nm YSZ-coated sample; the cross-sections of the air-side of e) the 50 nm YSZ-coated sample and f) the 200 nm YSZ-coated sample; and the cross-sections of the fuel-side of g) the 50 nm YSZ-coated sample and h) the 200 nm YSZ-coated sample, all of which were pre-oxidised for 20 min at 800 °C and exposed to the dual-atmosphere (Ar-5% H_2 + 3 % H_2O//Air + 3 % H_2O) for 1000 h at 600 °C. Insets: Higher-magnification images of selected scale regions.

side of the 50 nm CeO_2-coated sample shown in Fig. 3e, two microstructures are evident: the nodule, and the protective scale. The nodule is composed of an Fe-rich oxide top layer, roughly 10 μm in thickness, and underneath there is a spinel $(Fe,Cr)_3O_4$ with a thickness of approximately 5 μm. Underneath the spinel, an IOZ can be observed. The protective scale comprises a homogeneous and protective Cr-rich oxide (<100 nm) that covers the remainder of the sample surface. Fig. 3f depicts the cross-section of the air-side of the 200 nm CeO_2-coated sample. Features similar to those of the 50 nm CeO_2-coated sample are observed. The nodule is composed of an Fe-rich oxide of roughly 15 μm in thickness. Underneath the Fe-rich top layer, a roughly 10-μm-thick $(Fe,Cr)_3O_4$ spinel is observed, followed by an IOZ. The difference in thickness compared to the 50 nm CeO_2-coated sample is attributed to the fact that the nodule was not cut through its centre. The Cr-rich oxide (<100 nm) is similar to that observed on the 50 nm CeO_2-coated sample.

For both samples, the top-view images of the fuel-side (see Fig. 3c and d) show a homogeneous oxide scale with no apparent signs of corrosion. Fig. 3g shows the cross-section of the fuel-side of the 50 nm CeO_2-coated sample. A thin (<50 nm) and continuous Cr_2O_3 layer underneath the continuous CeO_2 coating are evident. The cross-section of the fuel-side of the 200 nm CeO_2-coated sample (Fig. 3h) shows a

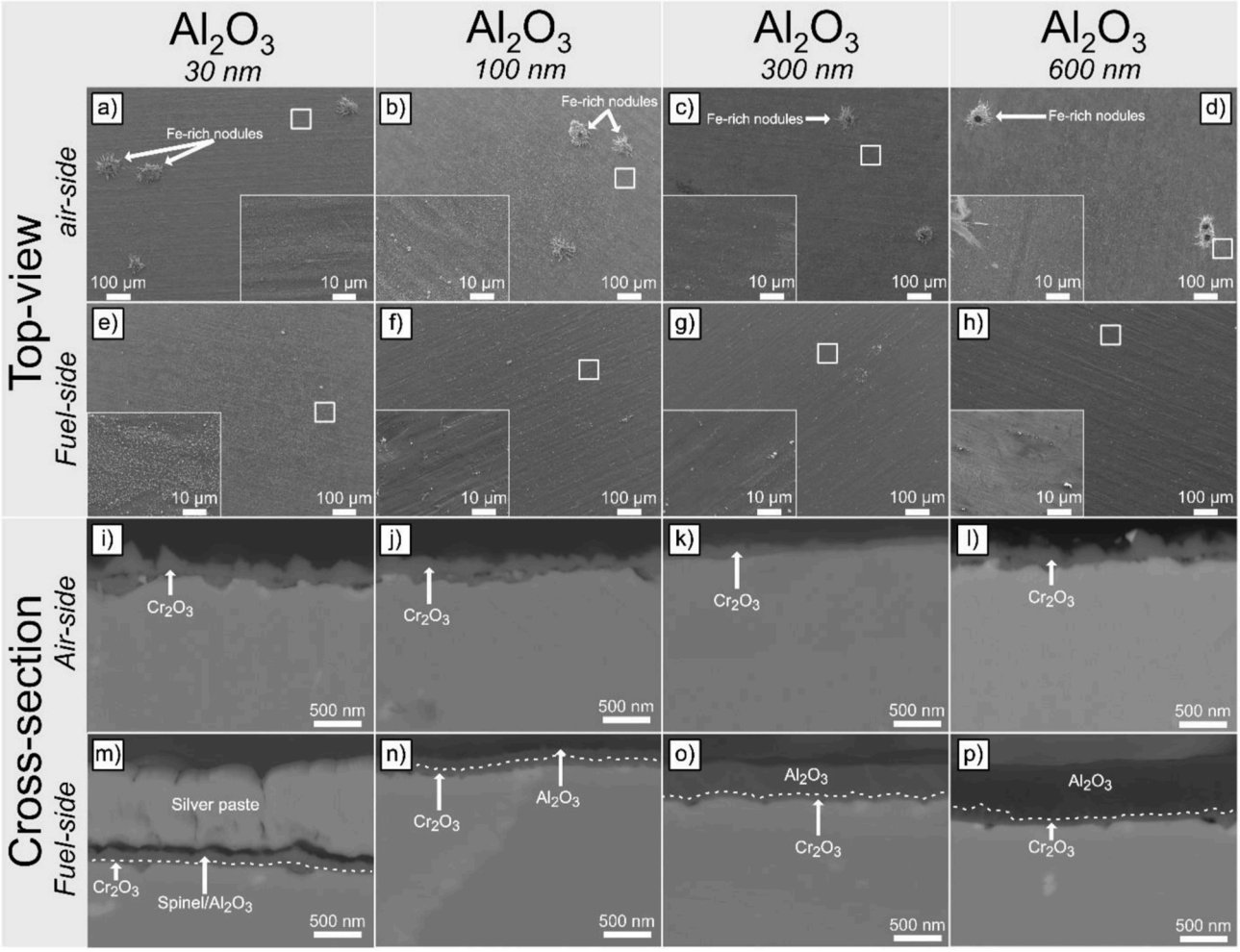

Fig. 5. SEM micrographs of Al_2O_3-coated samples representing the top-views of the air-side of: a) the 30 nm Al_2O_3-coated sample, b) the 100 nm Al_2O_3-coated sample, c) the 300 nm Al_2O_3-coated sample, and d) the 600 nm Al_2O_3-coated sample; the top-views of the fuel-side of: e) the 30 nm Al_2O_3-coated sample, f) the 100 nm Al_2O_3-coated sample, g) the 300 nm Al_2O_3-coated sample, and h) the 600 nm Al_2O_3-coated sample; the cross-sections of the air-side of: i) the 30 nm Al_2O_3-coated sample, j) the 100 nm Al_2O_3-coated sample, k) the 300 nm Al_2O_3-coated sample, l) and the 600 nm Al_2O_3-coated sample; and the cross-sections of the fuel-side of: m) the 30 nm Al_2O_3-coated sample, n) the fuel-side of the 100 nm Al_2O_3-coated sample, o) the fuel-side of the 300 nm Al_2O_3-coated sample, and p) the 600 nm Al_2O_3-coated sample, all of which were pre-oxidised for 20 min at 800 °C and exposed to the dual-atmosphere (Ar-5% H_2 + 3 % H_2O//Air + 3 % H_2O) for 3000 h at 600 °C. Insets: higher-magnification images of selected scale regions.

continuous CeO_2 layer on top of a thin (<50 nm) and continuous Cr_2O_3 oxide layer.

In summary, the 50 nm and 200 nm CeO_2-coated samples exhibit similar behaviour. Some nodules can be observed after 1000 h of exposure, although no severe breakaway oxidation is observed. Reactive elements (RE: Ce, Y, La etc.) are known to reduce the corrosion rate by changing the diffusion mechanism from outward diffusion of chromium to inward diffusion of oxygen [19,20]. Previous research [48] has shown that a thin layer of Ce drastically reduces the thickness of the Cr_2O_3 layer when exposed in air at 850 °C. Alnegren et al. [49] have shown that a thin layer of Ce (~10 nm) can reduce the chromia thickness by approximately a factor of three after exposure for 4500 h in Ar – 40 % H_2O – 3 % H_2 at 850 °C. In the present work, the Cr_2O_3 layer on the fuel-side of the CeO_2-coated samples (Fig. 3g and h) is approximately half as thick as the chromia layer observed on the fuel-side of the uncoated sample (see Fig. 2g), revealing a beneficial effect of Ce. An additional benefit of a cerium oxide coating on the fuel-side might be its efficiency as a diffusion barrier coating that prevents inter-diffusion between the ferritic steels and the nickel-rich anode or the contact paste, preventing austenization [50].

3.4. YSZ-coated steel

SEM micrographs of samples coated with either 50 nm or 200 nm of YSZ are shown in Fig. 4. Fig. 4a and b show the top-views of the air-side of the YSZ-coated samples. In both cases, the sample surface is covered mostly by a protective Cr-rich oxide scale, together with the presence of some Fe-rich nodules, which are approximately 80 µm in diameter for the 50 nm YSZ-coated sample, and 60 µm in diameter in the case of the 200 nm YSZ-coated sample. The cross-section of the air-side of the 50 nm YSZ-coated sample (see Fig. 4e) shows two different microstructures: an Fe-rich nodule, and the protective oxide scale. The nodule is composed of an Fe-rich oxide (~10 µm in thickness) on top and a (Fe, Cr)$_3O_4$ spinel underneath (~5 µm in thickness). An IOZ is visible under the spinel. A thin and homogeneous Cr-rich oxide, approximately 50 nm in thickness, is covering the remainder of the sample surface. Fig. 4f shows the cross-section of the air-side of the 200 nm YSZ-coated sample. A thin (<100 nm) and homogeneous Cr-rich oxide layer is covering the sample surface. The area fraction of the nodules is very low, which explains why no nodules are observed on the cross-section. It is likely that these nodules have the same microstructure as the nodule observed in the 50 nm YSZ-coated sample.

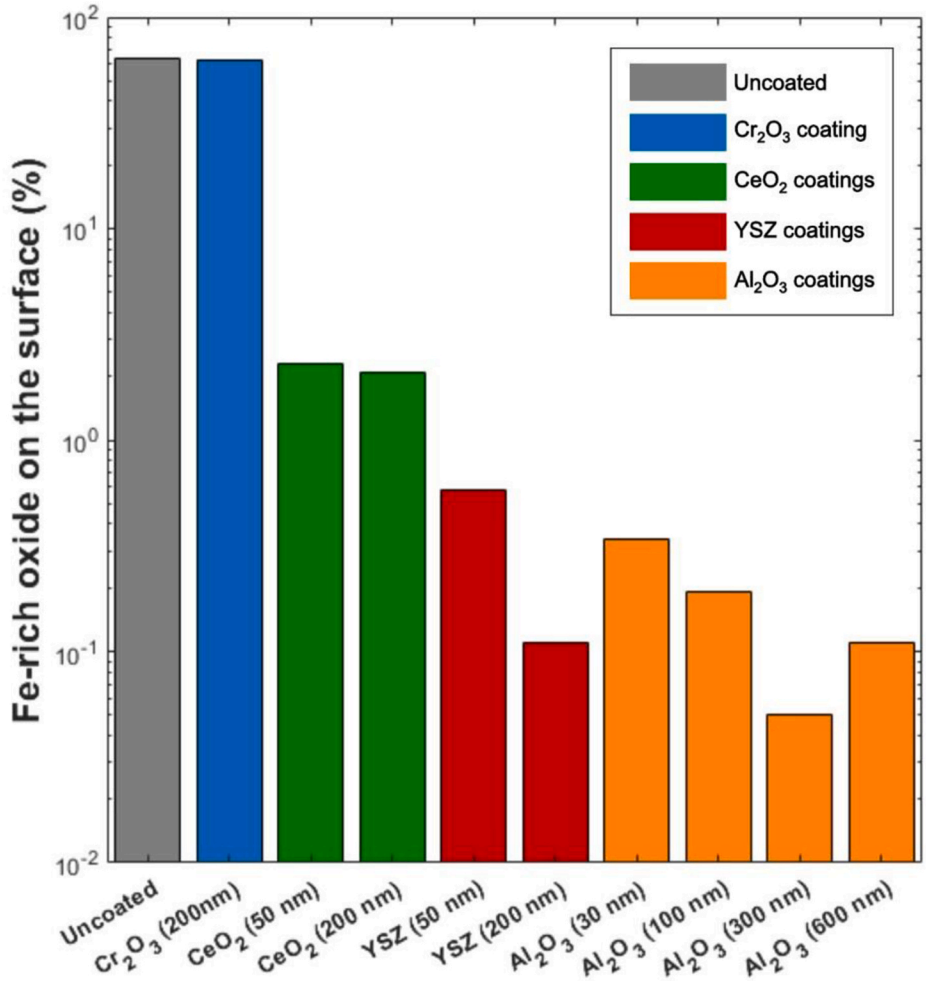

Fig. 6. Approximations of the extents of the Fe-rich phases covering the uncoated sample, Cr_2O_3-coated sample, CeO_2-coated sample, YSZ-coated sample exposed for 1000 h, and Al_2O_3-coated sample exposed for 3000 h under dual-atmosphere conditions (Ar-5% H_2 + 3 % H_2O//Air + 3 % H_2O) at 600 °C.

The cross-section of the fuel-side of the 50 nm YSZ-coated sample (Fig. 4g) shows a protective oxide scale. However, in Fig. 4h, the cross-section of the fuel-side of the 200 nm YSZ-coated sample shows micro-cracks in the coating, corresponding to approximately 20 % of the sample surface. The SEM image of the fuel-side (Fig. 4g) shows a thin YSZ oxide layer on top, followed by a thin Cr_2O_3 layer (<100 nm in thickness). The cross-section of the fuel-side of the 200 nm YSZ-coated sample (see Fig. 4h) shows the YSZ layer, which is approximately 200 nm thick. As observed in Fig. 4d, the coating is cracked. However, the cracks do not seem to penetrate the entire thickness of the coating. The YSZ coating is still approximately 50 nm thick, underneath the cracks. A thin Cr_2O_3 layer (<100 nm in thickness) is observed under the YSZ coating.

Yen et al. [51] studied a ZrO_2 coatings on AISI 430 and showed a drastic reduction of hydrogen permeation compared to uncoated sample. Hatano et al. [52] performed hydrogen permeation tests on ZrO_2 coated (180 nm) SS430 and confirmed its excellent hydrogen barrier properties. In their work, they identified defects such as grain boundaries as permeation pathways for hydrogen in ZrO_2. Better protection against the dual-atmosphere effect might be achieved with the 200 nm YSZ-coated sample if the coating was crack-free.

3.5. Alumina-coated steel

Since the Al_2O_3 coatings showed excellent protective behaviours after 1000 h, the exposures were prolonged to 3000 h. Fig. 5 shows SEM micrographs of the Al_2O_3-coated samples exposed for 3000 h. The top-view of the air-side (Fig. 5a–d) shows a protective oxide layer that covers most of the surface, as well as the presence of very few Fe-rich nodules. The nodule size seems to decrease with increasing coating thickness. The 30 nm Al_2O_3-coated sample exhibits nodules of approximately 100 μm in diameter, while the 600 nm Al_2O_3-coated sample exhibits nodules that are approximately 50–60 μm in diameter. The cross-sections of the air-side of the Al_2O_3-coated samples are shown in Fig. 5i-l. All the samples show a thin (<100 nm) and homogeneous Cr_2O_3 oxide layer. No nodules are evident in the cross-sections. However, the few nodules observed in the top-view image are believed to have the same composition as the nodules observed in previous studies of FeCr alloys exposed to dual-atmosphere conditions [23,33,43].

The top-view images of the fuel-facing side of the Al_2O_3-coated samples (Fig. 5e–h) show a protective Al_2O_3 oxide layer that covers the entire surface. In the case of the 30 nm Al_2O_3-coated sample, it appears that some spinel oxide has overgrown the Al_2O_3 coating. Some crystallites with apparently cubic facets can be observed on top of the surface, which are not visible with thicker Al_2O_3 coatings. The cross-sections of the fuel-side (Fig. 5m-p) of the Al_2O_3-coated samples show a thin and homogeneous Al_2O_3 layer on top and a thin Cr_2O_3 layer (<100 nm) underneath, for the 100 nm, 300 nm, and 600 nm Al_2O_3 coatings. In the case of the 30 nm Al_2O_3 coating, it is difficult to distinguish between the Cr_2O_3 layer and the mix of spinel and Al_2O_3 observed in the top-view image. No signs of spallation of the oxide scale are evident for the 100 nm, 300 nm, and 600 nm Al_2O_3-coated samples, indicating good

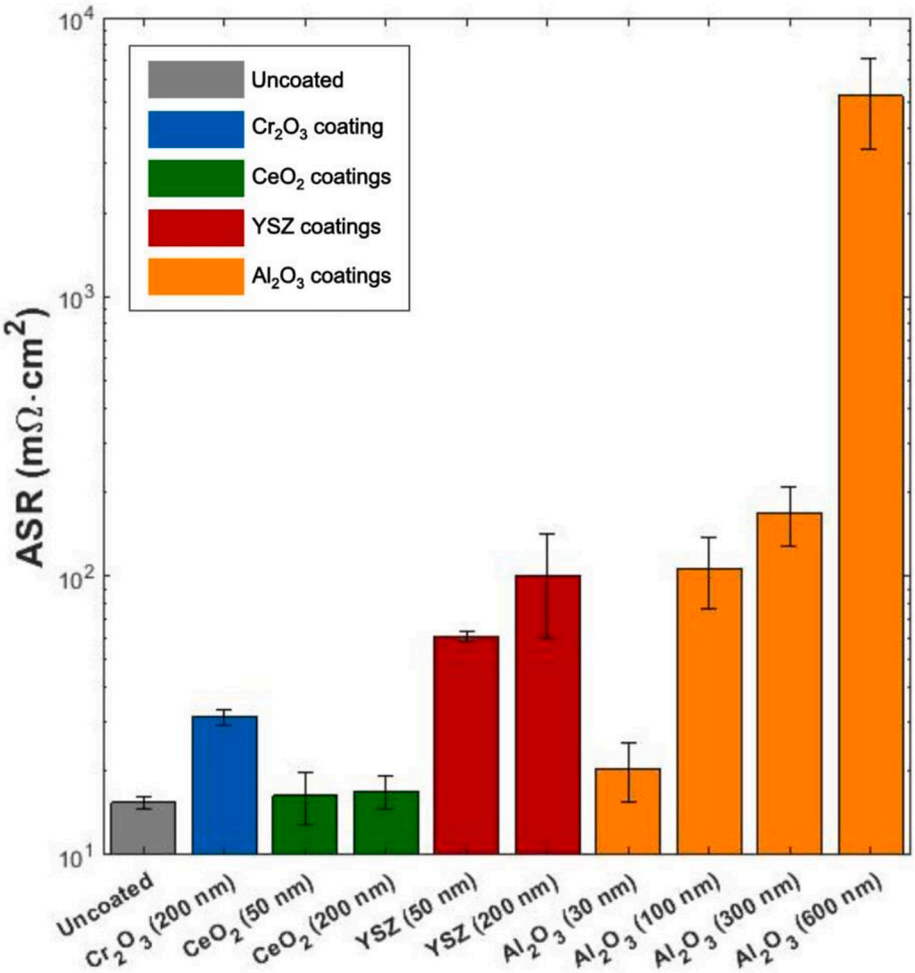

Fig. 7. ASR measurements performed in humid H_2 at 600 °C on uncoated, Cr_2O_3-coated, CeO_2-coated, YSZ-coated, and Al_2O_3-coated samples exposed for 500 h in Ar–5 % H_2 + 3 % H_2O at a flow rate of 400 sml•min^{-1}. The error bars represent the standard deviation.

adherence of the sputtered oxide. The 30-nm-coated sample shows some spallation that is localised to the edges. This is attributed to the clamping procedure.

The most-desirable phase for this application is expected to be α-Al_2O_3. Belonoshko et al. [53] suggested that hydrogen diffusion in the corundum structure occurs between energy minima position preferentially along the *c*-axis. Somjit et al. [54] attribute the excellent hydrogen barrier properties of α-Al_2O_3 to Al vacancies that trap hydrogen. In their study, it is also suggested that doping of the Al_2O_3 layer with Fe or Cr might reduce hydrogen permeability further.

Nevertheless, α-Al_2O_3 is known to form at much higher temperatures (>1000 °C) even if the formation of α-Al_2O_3 at lower temperatures (800 °C) has been reported [55]. In a previous study [43] a similar PVD-sputtered Al_2O_3 oxide layer (~500 nm in thickness) has been investigated by GI-XRD. Since no sign of α-Al_2O_3 was found the Al-oxide is considered amorphous.

3.6. Overview of the corrosion behaviour of the samples

Fig. 6 shows the estimations of the surface fractions covered by Fe-rich oxide for the samples exposed under dual-atmosphere conditions. As seen in the SEM micrographs of the uncoated and Cr_2O_3-coated samples (see Fig. 2), most of the surface of each sample is covered by a poorly protective Fe-rich oxide scale (~65 %), indicating a limited protective effect of the PVD chromia layer against the dual-atmosphere effect.

Both CeO_2-coated samples show similar and much lower percentages of non-protective oxide (~2 %), as compared to the uncoated and Cr_2O_3-coated samples, demonstrating a beneficial effect of CeO_2. However, an increase of the CeO_2 thickness has only a limited effect. The corrosion products are present in the form of nodules that are scattered over the surface; no continuous Fe-rich oxide layer is observed (see Fig. 1), as in contrast to uncoated and Cr_2O_3-coated samples.

The YSZ-coated samples show a further reduction in Fe-rich oxide coverage of the sample surface (~0.6 %–~0.1 %) compared to CeO_2 coatings. Previous research [56] has shown that YSZ is an effective hydrogen barrier. Matching with the observed resulting mild dual-atmosphere corrosion.

The Al_2O_3-coated samples, exposed for 3000 h instead of 1000 h, show a very low level of Fe-rich oxide formation (<0.3 %). There seems to be a beneficial effect of a thicker coating.

3.7. ASR measurements

The electrical conductivity of the coated interconnects directly impacts the eventual performance of a fuel cell. Therefore, the resistance value must be kept as low as possible and it should increase as little as possible over time. An ASR value of <100 mΩ cm^2 is commonly reported as an acceptable threshold for ASR [57]. Fig. 7 shows the ASR results measured in humid H_2 for the different coated samples after exposure in Ar – 5 % H_2 + 3 % H_2O for 500 h. On the uncoated "air" side, the oxide was removed. Uncoated samples exhibit an ASR of 15 mΩ cm^2 on

average, while Cr_2O_3-coated samples exhibit an ASR of 30 mΩ cm^2 on average. This correlates with the previous observation of Goebel et al. [9], who reported that the Cr_2O_3 layer is the main contributor to ASR. Uncoated samples exhibit a Cr_2O_3 layer that is approximately 100 nm in thickness, while Cr_2O_3-coated samples display an oxide layer that is 200 nm in thickness, which corresponds to roughly an increase of a factor of two for both the thickness and ASR value. CeO_2-coated samples, regardless of the coating thickness, exhibit a similar ASR value (16 mΩ cm^2). Previous studies [58,59] have shown that at low pO_2, CeO_2 becomes an n-type semi-conductor with considerable electronic conductivity. Xiong et al. [60] and Tuller et al. [61] have found that at 600 °C, pure CeO_2 exhibits a higher conductivity compared to Cr_2O_3 in the same conditions [62]. The measured ASR values are therefore, mainly determined by the Cr_2O_3 layer. CeO_2-coated samples exhibit a chromia layer thickness <100 nm, which corresponds approximately to the thickness observed for the uncoated sample (see Fig. 2g), hence similar ASR values are expected. YSZ-coated samples exhibit much higher ASR values than CeO_2-coated samples. YSZ is a rather poor electronic conductor [63], which is why it is used as an electrolyte material. YSZ-coated samples are approximately 3 to 4-times less conductive than CeO_2-coated samples. However, a thicker YSZ oxide scale does not seem to significantly increase the ASR. This is attributed to the surface state of the coating after the pre-oxidation step. As shown in Fig. 4d, the oxide layer is cracked, which may improve the overall conductivity. Alumina is known to be an insulator [64,65], which is in accordance with the obtained results. The Al_2O_3-coated (≥100 nm) samples show higher ASR values than the other coatings, while the 30 nm Al_2O_3-coated samples have only slightly higher ASR values than the uncoated and CeO_2-coated samples. This low ASR value for the 30 nm Al_2O_3-coated samples is attributed to the fact that pinholes in the coatings provide high-conductivity pathways.

The results suggest that once the Al_2O_3 thickness surpasses 100 nm, a continuous Al_2O_3 layer is established, and the ASR becomes prohibitively high. Overall, the ASR increases with Al_2O_3 thickness. The higher ASR value (~3.5 Ω cm^2) is found for the 600 nm Al_2O_3-coated samples. This is in agreement with previous research [43] reporting high ASR values for Al_2O_3-coated samples exposed under similar conditions.

4. Conclusions

Fuel-side coatings for interconnects have been studied in this work to evaluate their protective properties with respect to mitigating dual-atmosphere corrosion of Fe–Cr steel at 600 °C. The thermally grown Cr_2O_3 layer formed during 20 min of pre-oxidation is not sufficient to reduce the dual-atmosphere corrosion effect. Therefore, the use of coatings is necessary. The main findings of this work are as follows:

- Cr_2O_3 coating does not significantly improve the resistance of the steel towards the dual-atmosphere effect at the investigated exposure conditions.
- The CeO_2 coating greatly reduces the dual-atmosphere corrosion, as compared to uncoated and the Cr_2O_3 coated material. Furthermore, CeO_2. is a reasonably good electronic conductor at 600 °C and at low pO_2.
- YSZ provides much better protection against the dual-atmosphere effect than CeO_2 coatings. However, its poor electronic conductivity raises doubts as to its applicability.
- Al_2O_3 coatings act as effective hydrogen barriers resulting in protective behaviours on the air-side, even after 3000 h of exposure. However, due to the insulating properties of Al_2O_3, the ASR values are much higher. Thicker coatings result in higher ASR and better protectiveness.
- A thin Al_2O_3 coating (~30 nm) may provide a sufficient barrier against corrosion while the low thickness results in an acceptable ASR penalty.

The investigated coatings show that a trade-off between hydrogen barrier properties and ASR increase is required. The results indicate that CeO_2-based coatings or very thin Al_2O_3 coatings are the most promising candidates as fuel-side coatings.

Declaration of competing interest

The authors declare that they have no known competing financial interests or personal relationships that could have appeared to influence the work reported in this paper.

Acknowledgements

This work was conducted at the Swedish High Temperature Corrosion Centre (HTC) at Chalmers University of Technology. This work was performed in part at the Chalmers Material Analysis Laboratory, CMAL. The authors are grateful for funding received from the Swedish Energy Agency through the FFI program and the strategic innovation program Metalliska Material (VINNOVA grant no. 2021-01003), which is a joint program of VINNOVA, Formas, and the Swedish Energy Agency.

References

[1] Stambouli AB, Traversa E. Solid oxide fuel cells (SOFCs): a review of an environmentally clean and efficient source of energy. Renew Sustain Energy Rev 2002;6:433–55.
[2] Singhal SC. Solid oxide fuel cells: past, present and future. Solid Oxide Fuels Cells: facts and Figures. Springer; 2013. p. 1–23.
[3] Fergus J, Hui R, Li X, Wilkinson DP, Zhang J. Solid oxide fuel cells: materials properties and performance. CRC press; 2016.
[4] Brandon N. Solid oxide fuel cell lifetime and reliability: critical challenges in fuel cells. Academic Press; 2017.
[5] Reddy MJ, Svensson J-E, Froitzheim J. Reevaluating the Cr evaporation characteristics of Ce/Co coatings for interconnect applications. ECS Trans 2021; 103:1899.
[6] Froitzheim J, Canovic S, Nikumaa M, Sachitanand R, Johansson LG, Svensson JE. Long term study of Cr evaporation and high temperature corrosion behaviour of Co coated ferritic steel for solid oxide fuel cell interconnects. J Power Sources 2012; 220:217–27.
[7] Sachitanand R, Sattari M, Svensson J-E, Froitzheim J. Evaluation of the oxidation and Cr evaporation properties of selected FeCr alloys used as SOFC interconnects. Int J Hydrogen Energy 2013;38:15328–34.
[8] Reddy MJ, Svensson J-E, Froitzheim J. Evaluating candidate materials for balance of plant components in SOFC: oxidation and Cr evaporation properties. Corrosion Sci 2021;190:109671.
[9] Goebel C, Fefekos AG, Svensson J-E, Froitzheim J. Does the conductivity of interconnect coatings matter for solid oxide fuel cell applications? J Power Sources 2018;383:110–4.
[10] Molin S, Jasinski P, Mikkelsen L, Zhang W, Chen M, Hendriksen PV. Low temperature processed MnCo2O4 and MnCo1. 8Fe0. 2O4 as effective protective coatings for solid oxide fuel cell interconnects at 750 C. J Power Sources 2016;336: 408–18.
[11] Falk-Windisch H, Claquesin J, Sattari M, Svensson J-E, Froitzheim J. Co-And Ce/Co-coated ferritic stainless steel as interconnect material for intermediate temperature solid oxide fuel cells. J Power Sources 2017;343:1–10.
[12] Wang R, Sun Z, Pal UB, Gopalan S, Basu SN. Mitigation of chromium poisoning of cathodes in solid oxide fuel cells employing CuMn 1.8 O 4 spinel coating on metallic interconnect. J Power Sources 2018;376:100–10.
[13] Waluyo NS, Park S-S, Song R-H, Lee S-B, Lim T-H, Hong J-E, et al. Protective coating based on manganese–copper oxide for solid oxide fuel cell interconnects: plasma spray coating and performance evaluation. Ceram Int 2018;44:11576–81.
[14] Cheng F, Cui J, Wang L, Li S, Sun J. Performance of CoNiO spinel oxide coating on AISI 430 stainless steel as interconnect for intermediate temperature solid oxide fuel cell. Int J Hydrogen Energy 2017;42:12477–84.
[15] Canovic S, Froitzheim J, Sachitanand R, Nikumaa M, Halvarsson M, Johansson L-G, et al. Oxidation of Co-and Ce-nanocoated FeCr steels: a microstructural investigation. Surf Coating Technol 2013;215:62–74.
[16] Froitzheim J, Svensson J-E. Multifunctional nano-coatings for SOFC interconnects. ECS Trans 2011;35:2503.
[17] Zanchi E, Ignaczak J, Molin S, Cempura G, Boccaccini A, Smeacetto F. Electrophoretic co-deposition of Mn1. 5Co1. 5O4, Fe2O3 and CuO: unravelling the effect of simultaneous addition of Cu and Fe on the microstructural, thermo-mechanical and corrosion properties of in-situ modified spinel coatings for solid oxide cell interconnects. J Eur Ceram Soc 2022;42:3271–81.
[18] Falk-Windisch H, Claquesin J, Svensson J-E, Froitzheim J. The effect of metallic Co-coating thickness on ferritic stainless steels intended for use as interconnect material in intermediate temperature solid oxide fuel cells. Oxid Metals 2018;89: 233–50.

[19] Whittle D, Stringer J. Improvements in high temperature oxidation resistance by additions of reactive elements or oxide dispersions. Philosophical transactions of the royal society of London series A, mathematical and physical sciences, vol. 295; 1980. p. 309–29.
[20] Hou P, Stringer J. The effect of reactive element additions on the selective oxidation, growth and adhesion of chromia scales. Mater Sci Eng, A 1995;202: 1–10.
[21] Alman D, Jablonski P. Effect of minor elements and a Ce surface treatment on the oxidation behavior of an Fe–22Cr–0.5 Mn (Crofer 22 APU) ferritic stainless steel. Int J Hydrogen Energy 2007;32:3743–53.
[22] Naumenko D, Pint B, Quadakkers W. Current thoughts on reactive element effects in alumina-forming systems: in memory of John Stringer. Oxid Metals 2016;86: 1–43.
[23] Alnegren P, Sattari M, Svensson J-E, Froitzheim J. Severe dual atmosphere effect at 600 C for stainless steel 441. J Power Sources 2016;301:170–8.
[24] Alnegren P, Sattari M, Svensson J-E, Froitzheim J. Temperature dependence of corrosion of ferritic stainless steel in dual atmosphere at 600–800 C. J Power Sources 2018;392:129–38.
[25] Yang Z, Walker MS, Singh P, Stevenson JW. Anomalous corrosion behavior of stainless steels under SOFC interconnect exposure conditions. Electrochem Solid State Lett 2003;6:B35.
[26] Yang Z, Walker MS, Singh P, Stevenson JW, Norby T. Oxidation behavior of ferritic stainless steels under SOFC interconnect exposure conditions. J Electrochem Soc 2004;151:B669.
[27] Kurokawa H, Kawamura K, Maruyama T. Oxidation behavior of Fe–16Cr alloy interconnect for SOFC under hydrogen potential gradient. Solid State Ionics 2004; 168:13–21.
[28] Rufner J, Gannon P, White P, Deibert M, Teintze S, Smith R, et al. Oxidation behavior of stainless steel 430 and 441 at 800 C in single (air/air) and dual atmosphere (air/hydrogen) exposures. Int J Hydrogen Energy 2008;33:1392–8.
[29] Stygar M, Brylewski T, Kruk A, Przybylski K. Oxidation properties of ferritic stainless steel in dual Ar–H2–H2O/air atmosphere exposure with regard to SOFC interconnect application. Solid State Ionics 2014;262:449–53.
[30] Horita T, Kishimoto H, Yamaji K, Xiong Y, Sakai N, Brito ME, et al. Oxide scale formation and stability of Fe–Cr alloy interconnects under dual atmospheres and current flow conditions for SOFCs. J Electrochem Soc 2006;153:A2007.
[31] Horita T, Xiong Y, Yamaji K, Sakai N, Yokokawa H. Evaluation of Fe-Cr alloys as interconnects for reduced operation temperature SOFCs. J Electrochem Soc 2003; 150:A243.
[32] Gagliani L, Visibile A, Gündüz KÖ, Svensson J-E, Froitzheim J. The influence of humidity content on ferritic stainless steels used in solid oxide fuel cell under dual atmosphere conditions at 600° C. ECS Trans 2021;103:1809.
[33] Gunduz KO, Chyrkin A, Goebel C, Hansen L, Hjorth O, Svensson J-E, et al. The effect of hydrogen on the breakdown of the protective oxide scale in solid oxide fuel cell interconnects. Corrosion Sci 2021;179:109112.
[34] Nakagawa K, Matsunaga Y, Yanagisawa T. Corrosion behavior of ferritic steels on the air sides of boiler tubes in a steam/air dual environment. Mater A T High Temp 2003;20:67–73.
[35] Goebel C, Alnegren P, Faust R, Svensson J-E, Froitzheim J. The effect of pre-oxidation parameters on the corrosion behavior of AISI 441 in dual atmosphere. Int J Hydrogen Energy 2018;43:14665–74.
[36] Li J, Yan D, Gong Y, Jiang Y, Li J, Pu J, et al. Investigation of anomalous oxidation behavior of SUS430 alloy in solid oxide fuel cell dual atmosphere. J Electrochem Soc 2017;164:C945.
[37] Zhao Y, Fergus J. Oxidation of alloys 430 and 441 in SOFC dual atmospheres: effects of flow rate and humidity. J Electrochem Soc 2011;159:C109.
[38] Skilbred AWB, Haugsrud R. The effect of dual atmosphere conditions on the corrosion of Sandvik Sanergy HT. Int J Hydrogen Energy 2012;37:8095–101.
[39] Amendola R, Gannon P, Ellingwood B, Hoyt K, Piccardo P, Genocchio P. Oxidation behavior of coated and preoxidized ferritic steel in single and dual atmosphere exposures at 800 C. Surf Coating Technol 2012;206:2173–80.
[40] Reisert M, Anisur M, Lee L, Aphale A, Hong J, Yaginuma M, et al. Corrosion of chromia-forming and alumina-forming ferritic stainless steels under dual atmosphere exposure conditions. J Electrochem Soc 2021;168:111506.
[41] Essuman E, Meier G, Żurek J, Hänsel M, Quadakkers W. The effect of water vapor on selective oxidation of Fe–Cr alloys. Oxid Metals 2008;69:143–62.
[42] Alnegren P, Sattari M, Svensson J-E, Froitzheim J. Severe dual atmosphere effect at 600 °C for stainless steel 441. J Power Sources 2016;301:170–8.
[43] Tomas M, Visibile A, Svensson J-E, Froitzheim J. Novel coatings for protecting solid oxide fuel cell interconnects against the dual-atmosphere effect. Int J Hydrogen Energy 2023;48:18405–19.
[44] Kurokawa H, Oyama Y, Kawamura K, Maruyama T. Hydrogen permeation through Fe-16Cr alloy interconnect in atmosphere simulating SOFC at 1073 K. J Electrochem Soc 2004;151:A1264.
[45] Tveten B, Hultquist G, Norby T. Hydrogen in chromium: influence on the high-temperature oxidation kinetics in O2, oxide-growth mechanisms, and scale adherence. Oxid Metals 1999;51:221–33.
[46] Norby T, Haugsrud R. Dense ceramic membranes for hydrogen separation. Nonporous Inorganic Membranes; 2006. p. 1–48.
[47] Henager C. Hydrogen permeation barrier coatings. 2007. p. 181–90.
[48] Grolig JG, Froitzheim J, Svensson J-E. Coated stainless steel 441 as interconnect material for solid oxide fuel cells: oxidation performance and chromium evaporation. J Power Sources 2014;248:1007–13.
[49] Alnegren P. Corrosion of ferritic stainless steel interconnects for solid oxide cells–challenging operating conditions. Sweden: Chalmers Tekniska Hogskola; 2018.
[50] Froitzheim J, Niewolak L, Brandner M, Singheiser L, Quadakkers W. Anode side diffusion barrier coating for solid oxide fuel cells interconnects. J Fuel Cell Sci Technol 2010;7(3):031020.
[51] Yen SK, Huang IB, Yen ZS. Effects of electrolytic zirconium oxide coating on hydrogen permeation of AISI 430 stainless steel. Corrosion 2000;56:998–1004.
[52] Hatano Y, Zhang K, Hashizume K. Fabrication of ZrO2 coatings on ferritic steel by wet-chemical methods as a tritium permeation barrier. Phys Scripta 2011;2011: 014044.
[53] Belonoshko AB, Rosengren A, Dong Q, Hultquist G, Leygraf C. First-principles study of hydrogen diffusion in α-Al2O3 and liquid alumina. Phys Rev B 2004;69:024302.
[54] Somjit V, Yildiz B. Doping α-Al2O3 to reduce its hydrogen permeability: thermodynamic assessment of hydrogen defects and solubility from first principles. Acta Mater 2019;169:172–83.
[55] Josefsson H, Liu F, Svensson JE, Halvarsson M, Johansson LG. Oxidation of FeCrAl alloys at 500–900 C in dry O2. Mater Corros 2005;56:801–5.
[56] Nigara Y, Yashiro K, Hong J-O, Kawada T, Mizusaki J. Hydrogen permeability of YSZ single crystals at high temperatures. Solid State Ionics 2004;171:61–7.
[57] Piccardo P, Gannon P, Chevalier S, Viviani M, Barbucci A, Caboche G, et al. ASR evaluation of different kinds of coatings on a ferritic stainless steel as SOFC interconnects. Surf Coating Technol 2007;202:1221–5.
[58] Tuller H, Nowick A. Defect structure and electrical properties of nonstoichiometric CeO2 single crystals. J Electrochem Soc 1979;126:209.
[59] Naik I, Tien T-Y. Small-polaron mobility in nonstoichiometric cerium dioxide. J Phys Chem Solid 1978;39:311–5.
[60] Xiong Y-P, Kishimoto H, Yamaji K, Yoshinaga M, Horita T, Brito ME, et al. Electronic conductivity of pure ceria. Solid State Ionics 2011;192:476–9.
[61] Tuller HL, Nowick AS. Defect structure and electrical properties of nonstoichiometric CeO2 single crystals. J Electrochem Soc 1979;126:209.
[62] Holt A, Kofstad P. Electrical conductivity and defect structure of Cr2O3. II. Reduced temperatures (<~ 1000 C). Solid State Ionics 1994;69:137–43.
[63] Ikeda S, Sakurai O, Uematsu K, Mizutani N, Kato M. Electrical conductivity of yttria-stabilized zirconia single crystals. J Mater Sci 1985;20:4593–600.
[64] Arizumi T, Tani S. On the electrical conductivity of alumina. J Phys Soc Jpn 1950; 5:442–7.
[65] Schemmel R, Philipp L, Stringer J, Gordon R. Electrical properties of a polycrystalline alumina sample. Richland, WA (United States): Hanford Engineering Development Lab.; 1972.